© **D. Dietz, A. Binder**

Institute of Electrical Energy Conversion – Darmstadt, Technical University (Darmstadt, Germany)

BEARINGLESS PM SYNCHRONOUS MACHINE WITH ZERO-SEQUENCE CURRENT DRIVEN STAR POINT-CONNECTED ACTIVE MAGNETIC THRUST BEARING

Abstract: Common cylindrical bearingless drives require a separate thrust bearing, which is fed by a DC supply. Here, a technique is presented, which enables the feeding of the thrust bearing by an artificially generated zero-sequence current between the two star points of the two parallel windings in the bearingless PM synchronous machine. This way, no additional DC supply for an axial active magnetic bearing is needed. It is replaced by two three-phase inverters as stator winding supply, which are needed in any case to generate torque and lateral rotor force in the motor. This examination explains the technique of adapting the electric potential of the star points in two three-phase windings of the motor. The focus is on the determination of the operating area (maximum zero-sequence current and band width). It is constrained by the bearingless motor due to torque and lateral force ripple as well as additional eddy current losses. On the other hand, the DC link voltage and the modulation degree of the inverter for simultaneous motor operation as well as the bearing inductance limit the system dynamic. It is shown that the proposed technique is applicable for a modulation degree < 0.866, taking into account that other constraints by the bearingless machine and the inverter are mainly noncritical.

Keywords: Bearingless drive, combined winding, zero-sequence current, star point-connected thrust bearing, active magnetic bearing

INTRODUCTION

Active magnetic self-bearing motors, often referred to as bearingless motors (BM), combine two functions in a single device: the torque generation by an electric machine and the suspension force generation by an active magnetic bearing (AMB) [1, 2, 3]. BMs can be categorized mainly into two groups: First and most prominent, into motors, which generate lateral rotor forces but require a separate axial AMB [4–7]. Second, into motors which do not require an additional axial AMB. Among these, there are BMs which do not need an axial position control due to a disk-like and thereby self-stabilizing rotor [8–12]. Other topologies can actively generate
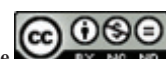
axial rotor force by a conical rotor [13, 14] or a chessboard structure on the rotor surface [15]. However, the complexity in terms of manufacturing effort and control disable these interesting solutions from industrial use. For lower power classes (< 500 W) also topologies are available, which passively stabilize the axial rotor position by means of several permanent magnet (PM) layers [16].

The predominant field of application for AMB-suspended drives is the use as high-speed drive because AMBs inherently mitigate the friction losses and enable the rotor rotation around its inertia axis to suppress vibration forces [1, 2, 17]. As such, small rotor diameters are necessary to keep the mechanical stress in the rotor at a suitable level. However, for these rotors, commonly cylindrical, a separate AMB for axial position control, a so-called thrust AMB, is required. Often the thrust bearing is realized parallel to a radial AMB as combined AMB [5] on the non-drive end (NDE) of the shaft, whereas the BM is mounted on the drive end (DE) in order to achieve a short axial length. But even if two BMs as two half-motors are used [18], an additional axial AMB is required. In any case, this axial AMB is usually fed by a DC chopper, which is costly.

Here, a technique is presented to avoid the additional DC supply. Therefore, it is made use of the fact that BMs typically are equipped with two star-connected winding systems. That means all the six motor terminals are used to generate torque, radial and axial force at the same time. In [19] it is shown that the electric scalar potential between the two star points Z_A and Z_B can be artificially adapted in order to generate a controllable current between Z_A and Z_B. Altogether, the
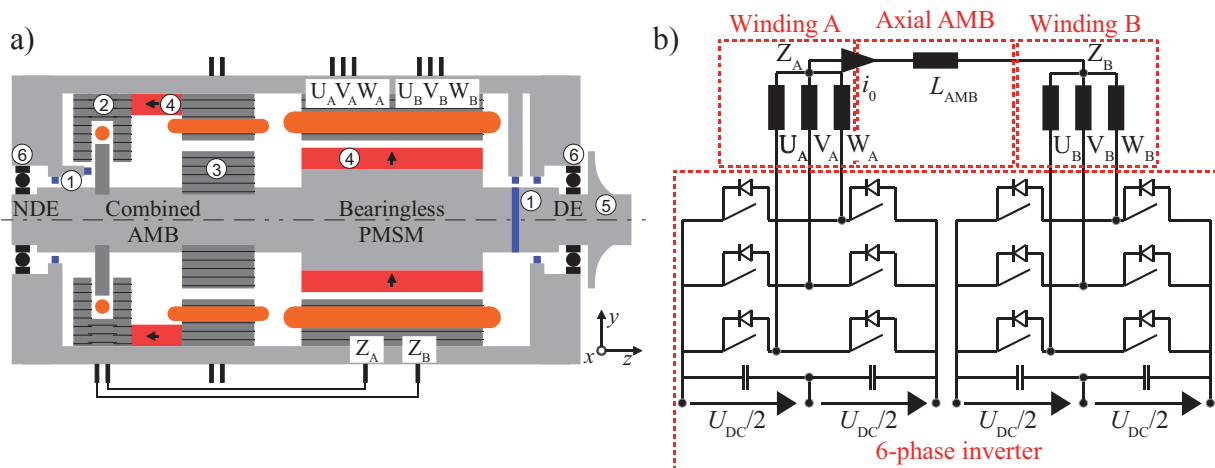
Fig. 1. Drive components (schematic) (1) Position and rotor angle sensors, (2) Axial part of combined AMB, (3) Radial part of combined AMB, (4) PM with magnetization direction, (5) Turbo-compressor wheel, (6) Safety bearings at drive and non-drive end (DE / NDE) a; simplified electric circuit of the bearingless machine and the axial AMB b

proposed technique is beneficial for high-speed bearingless motors with cylindrical rotors. A schematic overview of the drive system is given in Fig. 1a.

In the section "The bearingless PM synchronous machine" the bearingless machine is presented which the novel technique will be applied to. This is followed by the explanation of generating artificially a zero-sequence current system. The focus of the article is on the last two sections where the constraints inherently given by the motor and by the inverter are explained.

THE BEARINGLESS PM SYNCHRONOUS MACHINE

A prototype machine with a double three-phase winding was built which is similar to that in Fig. 1. In this prototype the thrust bearing is conventionally fed by a DC supply. It is not possible to apply the presented technique since the star points are insulated and not accessible. The function of this machine is, however, introduced shortly because the demonstrated principle refers to this machine topology. In [4, 20, 21] the winding topology as well as measuring results are presented in detail. Its main parameters are listed in Table 1. It is important to note that the technique is applicable for every bearingless machine which exhibits two three-phase windings fed by the same inverter.

Table 1. Motor specifications

Rated speed / min^{-1}	n_N	60 000
Rated torque / mNm	M_N	105
Rated lateral force / N	F_N	8.2
Rated phase voltage / V	$U_{s,N}$	42
Rated phase current for torque / A	$I_{cw,N}$	3.18
Rated phase current for lateral force / A	$I_{ccw,N}$	2.26
Rated total phase current / A	$I_{s,N}$	3.90
Rated current for axial force / A	$I_{0,N}$	0.9
Stator bore outer/inner diameter / mm	$d_{s,o}/d_{s,i}$	70/35
Stator stack length / mm	l_{Fe}	40
Bandage thickness / mm	h_b	1.5
Magnet height / mm	h_{PM}	2.75
Mechanical air gap $(d_{s,i} - d_{r,o})/2$ / mm	δ	1.0
Rotor mass / g	m_r	800
Number of turns per phase (6 phases)	$N_{s,6}$	22
Number of pole pairs (torque/suspension winding)	p/p_{sus}	1/2

In this machine a combined two-layer winding replaces the common drive and suspension windings. When accordingly fed it is possible to generate a field wave of pole count $2p = 2$, equal to the rotor field pole count, and a field wave of pole count $2p_{sus} = 2p + 2 = 4$ simultaneously. In interaction with the rotor field, the $2p$-pole field wave generates tangential force, whereas the $2p_{sus}$-pole field wave generates lateral force for rotor suspension. Starting from a conventional four-pole three-phase winding, this is possible if the winding per phase (e.g. phase U) is separated into two spatially opposed coil groups (e.g. U_A and U_B). Each of these coil groups is now fed by a separate phase yielding six phases consisting of the phase belt sequence $+U_A, +W_B, +V_A, +U_B, +W_A, +V_B$. The phase belts indexed by A (B) are referred to as three-phase system A (B). They are both star-connected, yielding the two star-points Z_A and Z_B. If the two systems are fed in phase a counter-clockwise rotating $2p_{sus}$-pole field wave occurs so that the phase sequence is reversed (i_{ccw}) for clockwise field wave rotation. If they are fed in phase opposition a clockwise rotating $2p$-pole field wave occurs by i_{cw}. In practice, both field waves are needed with clockwise rotation. So a superposition yields an elliptical current space vector orbit per three-phase system A and B consisting theoretically of two symmetrical three-phase current space vectors with reversed rotation [4, 20, 21]. This principle is used to realize the supply of the separate thrust bearing (inductance L_{AMB}) by an artificially generated current i_0 between the star points Z_A and Z_B. This is shown in Fig. 1b where U_{DC} is the DC link voltage of the inverter.

GENERATION OF THE REQUIRED ZERO-SEQUENCE VOLTAGE

The proposed technique relies on a conventional space vector pulse width modulation (SVPWM) [3]. That means, that for each of the elliptical three-phase current systems I_A and I_B a current controller determines a certain voltage space vector in the stator-fixed coordinate systems (α_A–β_A and α_B-β_B). This voltage requirement depends solely on the torque and radial suspension force requirement, whereas the axial force requirement is introduced at a later state. The amplitude of the applied phase voltages $\hat{u}_{A,s}$ and $\hat{u}_{B,s}$ which in the case of a symmetrical voltage system is equal to the length of the voltage space vectors $\underline{u}_A$ and $\underline{u}_B$ is limited by the hexagon in Fig. 2a. In this case, due to the superposition of the clockwise and counter-clockwise voltage system, the main axes of the ellipses determine the inverter voltage rating. These main axes are determined by the algebraic sum of the required clockwise and counter-clockwise rotating voltage space vectors for torque and lateral force generation. However, since the $2p$-pole rotor field does not induce into the imaginary $2p_{sus}$-pole suspension winding, the voltage trajectory is

only slightly elliptical, so that mainly the back-EMF of the $2p$-pole rotor field determines the voltage requirement as in common rotating field machines.

According to Fig. 2a the inverter states 0, …, 7 are related to the phase terminal electric potentials φ_U, φ_V and φ_W. They can take the discrete values $U_{DC}/2$ ($-U_{DC}/2$) when the related high-side switches are turned on (off). As the voltage space vector moves through the sectors I, …, VI (Fig. 2a) the adjoining inverter states are realized for a calculated time t_0, … t_7. For the traditional symmetrical SVPWM the calculation of t_0, … t_7 is well explained in literature [3, 22]. This technique is commonly used for three-phase inverters when operated in field-oriented control. It is important to note that only the time spans t_1, t_2 and $t_{passive}$ are mandatory for the torque and lateral force generation. The position of the time spans as well as the composition of $t_{passive}$ within one switching period, however, can be arbitrarily chosen. This is made use of for the here presented technique. The independent control of the zero-sequence voltage and the phase voltages by means of extended *Park* and *Clarke* transformations is discussed in in detail in [19]. The equivalent circuit of the current loop including the motor windings A and B and the axial AMB and defining the orientation of i_0 and u_0 is depicted in Fig. 2b. According to that the *Ohmic*-inductive voltage drop u_0 over the thrust AMB is dependent on the difference in electric potential between phase terminals $\varphi_{U,A}$, $\varphi_{V,A}$, $\varphi_{W,A}$ and $\varphi_{U,B}$, $\varphi_{V,B}$, $\varphi_{W,B}$. That is, every time a difference in potential between the star points occurs, a current is flowing if the star points are connected. This is inherently the case if the active voltage vectors in the two systems A and B are different ($t_{1,A} \neq t_{1,B}$ and $t_{2,A} \neq t_{2,B}$).
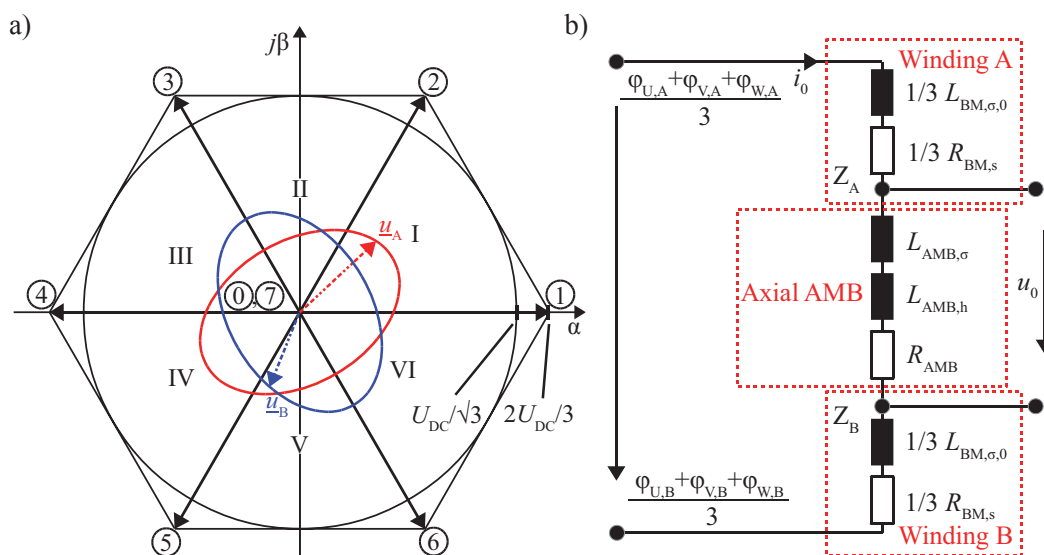
Fig. 2. Switching states (circled) and voltage space vector trajectories in the stator-fixed α-β-reference frame related to the voltage limit a; and equivalent circuit for the zero-sequence current component i_0 b

However, the overlapping time spans where a difference in potential is present can be influenced by variation of the time spans $t_{0,A}$, $t_{7,A}$, $t_{0,B}$ and $t_{7,B}$. Aside from the dependency of the difference in the star point potential also the relation between motor and AMB impedance as voltage divider k_{eq} (1) affects the maximum voltage over the terminals of the thrust AMB. Obviously the AMB impedance should be high in relation to the motor zero-sequence impedance for a dynamic current response. On the other hand, the overall impedance should be small for the same reason. The voltage at the AMB can be calculated according to (2) and can be written as (3), where $\overline{u}_0\big|_{T_{sw}}$ is the average voltage over one switching period T_{sw}.

$$u_0 \sim k_{eq} = \frac{3 \cdot (\omega L_{AMB,h} + \omega L_{AMB,\sigma} + R_{AMB})}{3 \cdot (\omega L_{AMB,h} + \omega L_{AMB,\sigma} + R_{AMB}) + 2 \cdot (\omega L_{BM,\sigma,0} + R_{BM,s})} \qquad (1)$$

$$\overline{u}_0\big|_{T_{sw}} = \frac{k_{eq}}{T_{sw}} \int_0^{T_{sw}} \left(\frac{\varphi_{U,A}(t) + \varphi_{V,A}(t) + \varphi_{W,A}(t)}{3} - \frac{\varphi_{U,B}(t) + \varphi_{V,B}(t) + \varphi_{W,B}(t)}{3} \right) dt \qquad (2)$$

$$\overline{u}_0\big|_{T_{sw}} = \frac{U_{DC} \cdot k_{eq}}{2 \cdot T_{sw}} \cdot \left(\underbrace{\frac{t_{2,A} - t_{1,A}}{3} + \frac{t_{1,B} - t_{2,B}}{3}}_{\substack{\text{Fixed time spans by different active} \\ \text{voltage vectors in system A and B}}} + \underbrace{\underbrace{t_{7,A} - t_{0,A} + t_{0,B} - t_{7,B}}_{\substack{\text{Controllable time spans for artificial} \\ \text{zero-seqence voltage generation}}}}_{t_{z,AMB}} \right) \qquad (3)$$

$$t_{passive,A} = t_{0,A} + t_{7,A} = T_{sw} - t_{active,A}; \quad t_{passive,B} = t_{0,B} + t_{7,B} = T_{sw} - t_{active,B} \qquad (4)$$

The time spans $t_{1,A}$, $t_{2,A}$, $t_{1,B}$ and $t_{2,B}$ are known since they are previously calculated. Therefore, up to now the parameters $\{t_{z,AMB}, t_{passive,A}, t_{passive,B}\} \in \mathbb{R}_3$ are known (3, 4) whereas the unknown parameters are $\{t_{0,A}, t_{7,A}, t_{0,B}, t_{7,B}\}$. To solve this under-determined system another condition has to be introduced. It is selected in a way that the overlapping time span $t_7 - t_0$ is proportional ($t_0 \to t_{0,lin}$, $t_7 \to t_{7,lin}$) to the relation between the time span for the passive voltage vectors of one system and the total time span for passive voltage vectors. From that system (5) results, which can be solved by applying *Cramer*'s rule. However, (5) yields solutions which can be both positive and negative. Therefore, the solution space must be limited to (6), resulting in a nonlinear switching behavior.

$$\begin{pmatrix} 1 & 1 & 0 & 0 \\ 0 & 0 & 1 & 1 \\ -1 & 1 & 1 & -1 \\ t_{passive,B} & -t_{passive,B} & t_{passive,A} & -t_{passive,A} \end{pmatrix} \cdot \begin{pmatrix} t_{0,A,lin} \\ t_{7,A,lin} \\ t_{0,B,lin} \\ t_{7,B,lin} \end{pmatrix} = \begin{pmatrix} t_{passive,A} \\ t_{passive,B} \\ t_{z,AMB} \\ 0 \end{pmatrix} \qquad (5)$$

$$\begin{cases} t_{0,A} = \dfrac{1}{2} \cdot \left(t_{\text{passive,A}} - \dfrac{t_{\text{passive,B}}}{t_{\text{passive,A}} + t_{\text{passive,B}}} \cdot t_{z,\text{AMB}} \right) & \forall \; t_{0,A,\text{lin}} > 0 \\[2mm] t_{0,A} = 0 \;\wedge\; t_{7,A} = t_{\text{passive,A}} & \forall \; t_{0,A,\text{lin}} < 0 \end{cases} \tag{6a}$$

$$\begin{cases} t_{7,A} = \dfrac{1}{2} \cdot \left(t_{\text{passive,A}} + \dfrac{t_{\text{passive,B}}}{t_{\text{passive,A}} + t_{\text{passive,B}}} \cdot t_{z,\text{AMB}} \right) & \forall \; t_{7,A,\text{lin}} > 0 \\[2mm] t_{7,A} = 0 \;\wedge\; t_{0,A} = t_{\text{passive,A}} & \forall \; t_{7,A,\text{lin}} < 0 \end{cases} \tag{6b}$$

$$\begin{cases} t_{0,B} = \dfrac{1}{2} \cdot \left(t_{\text{passive,B}} + \dfrac{t_{\text{passive,A}}}{t_{\text{passive,A}} + t_{\text{passive,B}}} \cdot t_{z,\text{AMB}} \right) & \forall \; t_{0,B,\text{lin}} > 0 \\[2mm] t_{0,B} = 0 \;\wedge\; t_{7,B} = t_{\text{passive,B}} & \forall \; t_{0,B,\text{lin}} < 0 \end{cases} \tag{6c}$$

$$\begin{cases} t_{7,B} = \dfrac{1}{2} \cdot \left(t_{\text{passive,B}} - \dfrac{t_{\text{passive,A}}}{t_{\text{passive,A}} + t_{\text{passive,B}}} \cdot t_{z,\text{AMB}} \right) & \forall \; t_{7,B,\text{lin}} > 0 \\[2mm] t_{7,B} = 0 \;\wedge\; t_{0,B} = t_{\text{passive,B}} & \forall \; t_{7,B,\text{lin}} < 0 \end{cases} \tag{6d}$$

Altogether, the active inverter switching instants can be calculated according to [3], whereas the passive inverter states are given by (6). However, the time spans of the two systems are coupled by (6) so that a common module for a three-phase inverter must be replaced by a novel six-phase module.

CONSTRAINTS BY THE BEARINGLESS MOTOR

If the two windings A and B are fed by a DC current as described above the M.M.F. distribution $V(\gamma,t)$ normal to the stator surface for the considered PM synchronous machine results as to see in Fig. 3. It is important to note that the current through the axial AMB is only one third in each phase, following *Kirchhoff*'s law (see Fig. 2 b)). From that it can be concluded that, aside from the symmetrical three-phase systems i_{cw} and i_{ccw}, the zero-sequence component $i_0(t)$ introduces field harmonics of order $v = 3, 9, 15, \dots$ according to (9). This field distribution does not move but is constant if i_0 is constant and pulsates with f_{ax} if i_0 is sinusoidal and f_{ax}-frequent.

$$V_v(\gamma,t) = \sum_{v=3,9,15,\dots}^{\infty} \frac{4}{\pi} \cdot \frac{1}{v} \cdot m \cdot N_c \cdot \frac{i_0(t)}{3} \cdot \cos(v \cdot \gamma); \quad N_c: \text{number of coil turns} \tag{9}$$
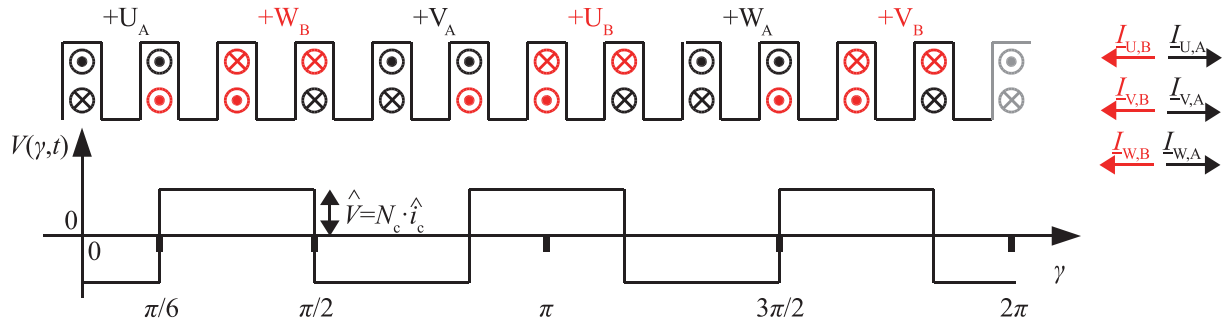
Fig. 3. M.M.F.-distribution $V(\gamma,t)$ normal to the stator surface at the stator inner bore (circumferential angle γ) for a pure zero-sequence current feeding $i_0(t)$, where coil current $i_c(t) = i_0(t)/3$ and coil turn count is N_c

Especially the third harmonic ($v = 3$) is harmful since higher harmonics only account for 2 % of the total field normal to the stator surface. The resulting field has to be taken care of for two reasons. First, like in a transformer, it induces a voltage in the phase winding due to a certain zero-sequence inductance $L_{BM,\sigma,0}$. This inductance together with the phase resistance forms a voltage divider according to (Fig. 2b). Therefore, it is desirable to keep the motor zero-sequence impedance low. However, for the given system the zero-sequence motor inductance $L_{BM,\sigma,0} = 57$ µH is negligible compared to the AMB inductance $L_{AMB} = 15$ mH (both from 2D finite element (FE) simulation by means of the software *JMAG*, winding overhang inductance analytically calculated). The second harmful influence of the six-pole field distribution is on the motor operation and treated hereafter. It yields torque ripple, force ripple and eddy current losses in the PM.

For all these fields of interest the worst case is active for a pure DC current feeding as shown in Fig. 4, 5. That means, the field distribution in Fig. 3 does not pulsate but is constant. The influence of the zero-sequence current on the *Ohmic* losses in the conductors is negligible and, thus, not considered here.

Torque ripple

The impact of the zero-sequence current on the torque ripple w_M is estimated analytically and via 2D FE simulation (Fig. 4). First, the analytical calculation process is shown in order to explain the origin of the torque ripple. It relies on the 2D *Maxwell* stress tensor $(f_r, f_t)^T$ (r: radial, t: tangential) in cylindrical coordinates and uses the assumptions of infinite iron permeability as well as neglection of the slotting, curvature and end effect.

The field wave of the vth stator and the μth rotor harmonic with respect to the circumferential angle γ of the stator field $B_{s,v}(\gamma,t)$ as well as of the rotor $B_{r,\mu}(\gamma,t)$ are superimposed at each time and are integrated over a closed surface in the air gap

(stack length l_{Fe}). This yields the time depending torque $M(t)$ (10, 11); N_s: Number of turns per phase, $k_{w,v}$: winding factor of vth harmonic, m: phase count, $r_{s,i}$: bore radius, i: torque harmonic order.

$$M(t) = \int_0^{l_{Fe}} \int_0^{2\pi} (f_t(\gamma, t) \cdot r_{s,i}) d\gamma dz = \tag{10}$$

$$= M_1 \cdot \sin(\varphi_{r,1} - \varphi_{s,1}) + \sum_{i=3,9,15,\dots}^{\infty} \hat{M}_i \cdot \sin(i \cdot \omega_s t + i \cdot \varphi_{r,i} - \varphi_{s,i})$$

From that, it can be concluded that apart from the well-known constant term an additional time-depending component is present. This component is of sinusoidal character, oscillating with frequencies $i \cdot \omega_s$ ($i = v = \mu$) according to the product of synchronous frequency ω_s and order of magnetic field space harmonics of equal pole count $v = \mu = 3, 9, 15, \dots$ excited by the zero-sequence current i_0. Here, most crucially the harmonic $v = \mu = 3$ produces a non-constant torque, oscillating with frequency $3 \cdot f_s$. One option to get rid of any torque ripple of this nature is to improve the magnetization pattern so that the PM excites a field distribution which is purely sinusoidal ($\hat{B}_{r,\mu} = 0 \ \forall \ i \neq \mu$).

From (10) the torque coefficients M_i can be calculated according to (11). From that, the low influence of a zero-sequence feeding can be seen. Equation (11) is valid for $m = 3$ phases. The analytical result (*Analyt. DC-current*) for the third harmonic current ripple is proved at rated operation by the FE simulation (*FE DC-current*) results from Fig. 4b.

$$M_1 = \hat{i}_{cw} \cdot k_{w,1} \cdot 2 \cdot m \cdot N_s \cdot \hat{B}_{r,1} \cdot l_{Fe} \cdot r_{s,i} \ ; \ M_{1,N} = 124.956 \ \text{mNm}$$

$$\hat{M}_i = \frac{i_0}{3} \cdot k_{w,i} \cdot 2 \cdot m \cdot N_s \cdot \hat{B}_{r,\mu=i} \cdot l_{Fe} \cdot r_{s,i} \ ; \ \hat{M}_{3,N} = 0.096 \ \frac{\text{mNm}}{\text{A}} \cdot i_0 \tag{11}$$

$$\Rightarrow w_M = 0.077 \ \frac{\%}{\text{A}}; \quad w_M = \left| \frac{M_{max} - M_{min}}{M_{max} + M_{min}} \right|$$

So far the zero-sequence current was assumed to be constant. However, sometimes due to mechanical imbalance and external force disturbances the axial force requirement as well as the linked current $i_0(t)$ is not constant. The calculation is not shown here, but it can be concluded that a time variant zero-sequence current introduces new frequencies in the torque harmonic spectrum. This can be harmful if certain resonances are excited by these frequencies. However, the force ripple (*FE AC-current*, Fig. 4b) is smaller in any case compared to the DC feeding. Fig. 4b shows the torque ripple amplitude for different zero-sequence current feedings ($\hat{i}_0 = 0 \dots 10.5$ A) at rated operation. For usual operation no more than $i_0 = °1$ A

($i_0/3 <{}^\circ 0.33$ A) is needed. From Fig. 4b it can be concluded that a zero-sequence feeding to this extent has no crucial influence on the torque ripple, staying below 0.2 %.

Force ripple

The origin of the ripple w_F in the lateral force is explained equivalent to the torque ripple calculation. To do so the *Maxwell* stress tensor $(f_r, f_t)^T$ has to be evaluated, taking into account that the force in the *x-y* coordinate system is needed for control purpose. In the calculation, stator and rotor field harmonics of order $v, \mu > 3$ are neglected for clarity since their influence is very small. The composition of the active lateral force is depicted in (12).

$$
\begin{aligned}
F_x(t) &= F_{op} \cdot \cos(\varphi_{r,1} - \varphi_{s,2}) + F_{dis} \cdot \cos(\varphi_{s,1} - \varphi_{s,2}) + \\
&+ \hat{F}_{var,1} \cdot \cos(\omega_s t + \varphi_{s,2} - \varphi_{s,3}) + \hat{F}_{var,2} \cdot \cos(2 \cdot \omega_s t - \varphi_{s,2} + 3 \cdot \varphi_{r,3}) \\
F_y(t) &= F_{op} \cdot \sin(\varphi_{r,1} - \varphi_{s,2}) + F_{dis} \cdot \sin(\varphi_{s,1} - \varphi_{s,2}) - \\
&- \hat{F}_{var,1} \cdot \sin(\omega_s t + \varphi_{s,2} - \varphi_{s,3}) + \hat{F}_{var,2} \cdot \sin(2 \cdot \omega_s t - \varphi_{s,2} + 3 \cdot \varphi_{r,3})
\end{aligned}
\tag{12}
$$

From (12) it can be seen that the lateral force in one distinct direction consists of four components whereof two are constant. The force coefficients can be calculated according to (13). Equation (13) is valid for $m = 3$ phases. The result is proved by FE simulations (see Fig. 4a). The two constant components cover the force component F_{op}, necessary for operation, and the component F_{dis}, representing the disturbing influence of the stator drive field by i_{cw} on the stator suspension field by i_{ccw}. The latter is not further discussed here.

$$
F_{op} = -\frac{1}{2} \cdot \hat{i}_{ccw} \cdot k_{w,2} \cdot 2 \cdot m \cdot N_s \cdot \hat{B}_{r,1} \cdot l_{Fe} \left(\frac{r_{s,i}}{p_{s,2} \cdot \delta} + 1 \right); \quad \left| F_{op,N} \right| = 8.584 \text{ N}
$$

$$
\hat{F}_{var,1} = \hat{i}_{ccw} \cdot \frac{i_0}{3} \cdot k_{w,2} \cdot k_{w,3} \cdot m^2 \cdot N_s^2 \cdot \mu_0 \cdot l_{Fe} \left(\frac{r_{s,i}}{9 \cdot \delta^2 \cdot \pi} - \frac{2}{3 \cdot r_{s,i} \cdot \pi} + \frac{1}{9 \cdot \delta \cdot \pi} \right);
$$

$$
\left| \hat{F}_{var,1,N} \right| = 0{,}0073 \, \frac{\text{N}}{\text{A}} \cdot i_0 \rightarrow w_{F,1,N} = 0{,}085 \, \frac{\%}{\text{A}}; \quad w_F = \left| \frac{F_{max} - F_{min}}{F_{max} + F_{min}} \right|
\tag{13}
$$

$$
\hat{F}_{var,2} = -\hat{i}_{ccw} \cdot k_{w,2} \cdot m \cdot N_s \cdot \hat{B}_{r,3} \cdot l_{Fe} \left(\frac{r_{s,i}}{p_{s,2} \cdot \delta} - 1 \right);
$$

$$
\left| \hat{F}_{var,2,N} \right| = 0{,}021 \text{ N} \rightarrow w_{F,2,N} = 0{,}25 \, \%
$$

a)   b)
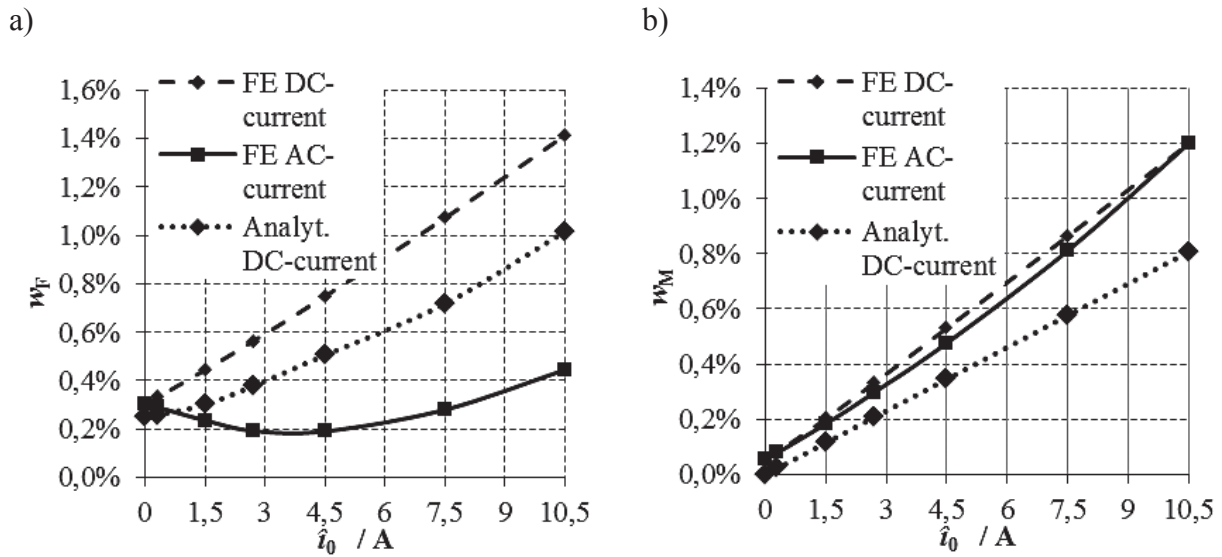
Fig. 4. Calculated force ripple w_F a; calculated torque ripple w_M b for different zero-sequence current feedings at $n_N = 60000$ min^{-1}, $M_N = 105$ mNm, FE: results from FE simulation (*JMAG*), AC feeding at $\omega_{ax} = \omega_s$; Other operating points behave similarly

Of importance are the two time variant components $F_{var,1}$ and $F_{var,2}$. $F_{var,1}$ is excited by the interaction between the constant six-pole field wave by i_0 and the rotating four-pole field wave by $i_{ccw}(t)$. The force generation results from the difference in pole count by ± 2. However, one field wave is caused by a f_s-frequent current $i_{ccw}(t)$, whereas the other results from a DC current i_0. From this difference the force ripple frequency is $f_{F,var,1} = f_s - 0 = f_s$. The amplitude is proportional to the zero-sequence current i_0 (13). For rated operation this force ripple is $w_{F,1,N} < 0.1\ \%$ (13) and not crucial compared to other disturbing influences. The second time variant component $F_{var,2}$ results from the third rotor field harmonic, rotating with synchronous velocity $v_{syn} = f_{r,\mu}/\mu$ and, therefore, $f_{r,3} = 3 \cdot f_s$ in case of a not purely sinusoidal magnetization in interaction with the four pole stator field wave, excited by the f_s-frequent current $i_{ccw}(t)$. From this difference the force ripple frequency is $f_{F,var,2} = 3 \cdot f_s - f_s = 2 \cdot f_s$. This force ripple is in effect even if no zero-sequence current is fed. It dominates the ripple of $F_{var,1}$ for values of $i_0 < 3$ A (13). The calculation with a time variant zero-sequence current is not shown here. It can introduce new frequencies in the lateral force spectrum that may be harmful. However, for the often considered case ($n \propto f_s \propto \omega_{ax}$) it can be seen that no force ripple harmonic is introduced.

From Fig. 4a it can be concluded that a zero-sequence feeding to this extent has no crucial influence on the force ripple, staying below 0.5 %. That means, the force ripple is mostly dominated by the $2 \cdot \omega_s$-frequent part $F_{var,2}$, which is caused by the 3rd rotor field harmonic ($\mu = 3$).

Eddy current losses in the PM

Generally, every stator-excited magnetic field wave differing from the operating wave induces voltages in eddy current loops formed by the conductive permanent magnet material due to the difference in rotational speed. Keeping the losses caused by these eddy currents low yields low rotor losses. This is a well-known design goal for many reasons [26]. Therefore, the following section shows the criticality of the zero-sequence current with respect to its induced eddy current losses in the PM. To understand the process a 2D analytical eddy current calculation in the form of a multilayer travelling-wave problem was carried out first. For simplicity it was made for a planar geometry. The analytical calculation of eddy current losses in the form of multilayer travelling-wave problems has been extensively discussed in literature [26–28]. The calculation process is elaborate and not shown here. The results from this calculation are shown in Table 2 and compared with the 2D FE simulation results under the same assumptions.

Table 2. Calculated eddy current losses in the rotor for the simplified 2D planar geometry (κ_{PM} = 1.25 Ms·m^{-1}, κ_{shaft} = 1.92 Ms·m^{-1}, $\mu_{r,PM}$ = 1, $\mu_{r,shaft}$ = 100)

Harmonic v	Machine part	Analytical	FE
2 ($\hat{\imath}_{ccw}$ = 3,2 A)	PM	2.61 W	2.55 W
	shaft	0.79 W	0.58 W
3 ($i_0/3$ = 1 A)	PM	0.52 W	0.51 W
	shaft	0.08 W	0.11 W
3 ($i_0/3$ = 3,5 A)	PM	6.33 W	6.32 W
	shaft	1.04 W	1.08 W

The results from the simplified 2D Cartesian geometry show the same tendency as the results from the 2D cylindrical geometry (Fig. 5). If less than 1 A zero-sequence current per phase ($i_0 < 3$ A) is injected, there are no relevant additional losses in the rotor of the machine. However, from 1 A the losses increase quickly according to $I^2 \cdot R$. Consequently a bearing current of $i_0 < 3$ A is not crucial and is seen to be the upper limit for the operating current, i.e. $i_{0,max}$ = 3 A (see Fig. 15).

CONSTRAINTS BY THE INVERTER

This section focuses on the dependency between the bearing performance and the operation point of the PWM-operated MOSFET inverter. Generally, one important design goal of the magnetic suspension control to ensure stability is
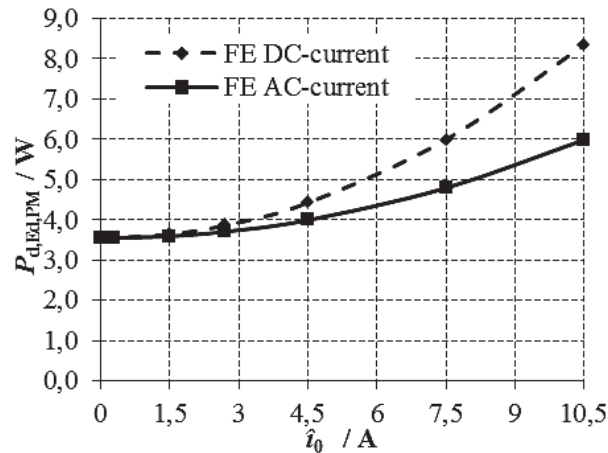
Fig. 5. Calculated eddy current losses $P_{d,Ft,PM}$ in the permanent magnets for different zero-sequence current feedings at rated operation ($n_N = 60000$ min^{-1}, $M_N = 105$ mNm) from 2D FE simulations (*JMAG*); other operating points show similar characteristics

the sufficiently fast change rate of the bearing current which is influenced by the required current amplitude, the frequency and voltage rating of the inverter as well as of the bearing inductance. In this case the amplitude of the current is limited by the motor tolerance for a zero-sequence current ($i_{0,max} = 3$ A). The frequency range and voltage amplitude of the current is limited by the inverter ($U_{DC,max} = 150$ V, $f_{sw,max} = 60$ kHz). Apart from these given parameters, the system design-related time constant of the plant ($\tau_{plant} = 10.64$ ms, see Fig. 2b) plays an important role. The choice of the desired parameters for a stiff control is limited in reality. Given the time constant of the plant and staying within the tolerance range of the zero-sequence current for the motor it is mainly dependent of the inverter.

In addition to this general statement, the difficulty has to be treated that the inverter capacity is constrained by the generation of the torque and suspension field in the bearingless motor. As can be seen from the switching instant calculation (section "Generation of the required zero-sequence voltage"), the generation of the two voltage systems is treated with priority. In accordance with that, it can be shown by simulation that neither in steady state nor in transient condition the zero-sequence voltage changes its time harmonic spectrum of the torque and lateral force generating motor currents. On the other hand, the operation point of the motor, determining the inverter operation point, influences the zero-sequence current slope and the axial bearing performance. Different points of operation that show this crucial impact are investigated by means of the software *Simulink* assuming ideal switching behavior in the following order: variable bearing current step response at rated motor operation, fixed bearing current step response at variable motor speed, inherent zero-sequence current with and without control, operating area for variable sinusoidal bearing current.

Variable bearing current step response at rated motor operation

Fig. 6 gives insight into the transient behavior of the bearing current for rated motor operation. In this and the following time plots $i_{0,\text{ideal}}$ gives the theoretical current in case of a pure DC voltage feeding $u_{0,\text{ideal}}$ (ideal inverter behavior, no PWM). i_0 and u_0 are the real current and real voltage, resulting from the pulse width modulated inverter.

In Fig. 6a it can be seen that current follows within 0.3 ms in comparison with the ideal case where the current follows within 0.1 ms. In this scenario the inverter shows the well-known lack element behavior. For a reference step of $i_{0,\text{ref}}$ = 3 A (Fig. 6b) the current follows within 0.9 ms which is again three times the time span of the pure DC voltage feeding. Further, the non-linear behavior which results from the zero-voltage time span calculation can be seen. However, it is already can be shown that the disturbing effect of the inverter on the controller circuit is acceptable for current requirements i_0 < 1 A.
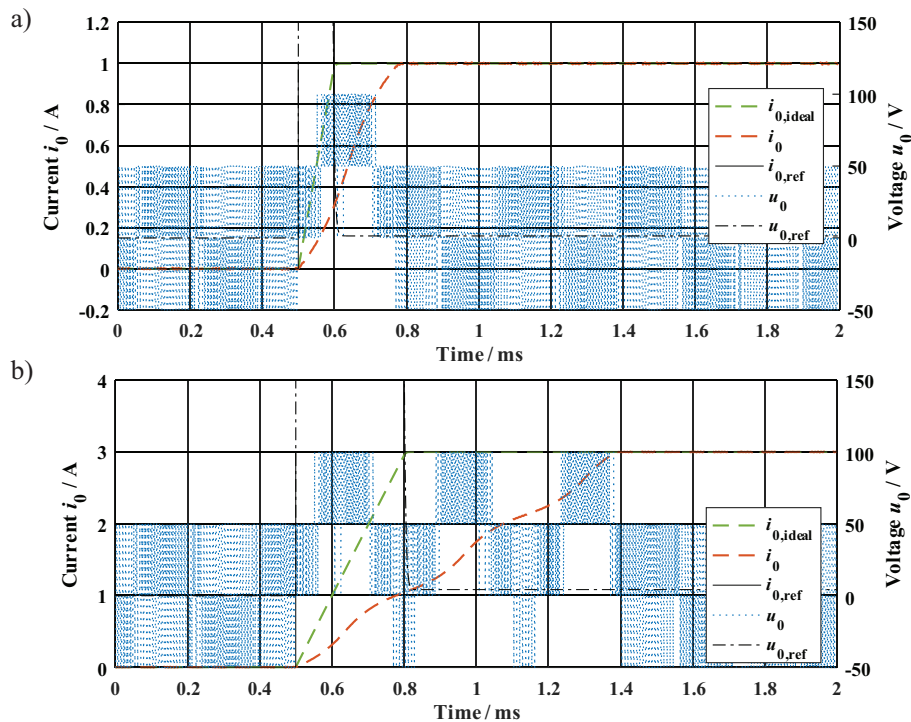
Fig. 6. Simulated step response response for a reference current step of $i_{0,\text{ref}}$ =1 A a; and $i_{0,\text{ref}}$ =3 A b; 0.5 ms at rated motor operation ($f_{s,N}$ = 1000 Hz, $\hat{U}_{cw}$ = 60 V, $\hat{U}_{ccw}$ = 3.2 V, f_{sw} = 60 kHz)

Fixed bearing current step response at variable motor speed

The influence of the inverter utilization by the motor operation, i.e. the modulation degree given by the back-EMF related motor speed, on the bearing

current slope has to be considered. This question is directly linked to the provided zero-voltage time spans which can be used in order to generate the zero-sequence current artificially. Therefore, Fig. 7 compares the zero-voltage duty states $d_{0,A}$, $d_{7,A}$, $d_{0,B}$, $d_{7,B}$ for Fig. 6a $n/n_N = 2/3$ and Fig. 6b $n/n_N = 4/3$.
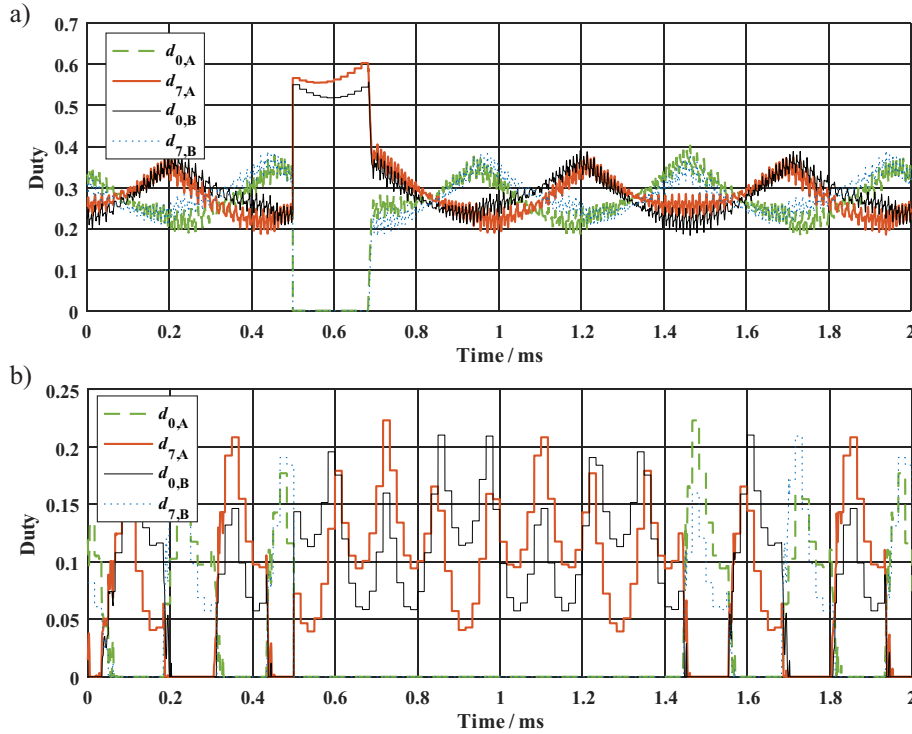
Fig. 7. Simulated zero-voltage duty states $d_{0,A}$, $d_{7,A}$, $d_{0,B}$, $d_{7,B}$, for a reference current step of $i_{0,ref} = 1$ A at 0.5 ms at rated suspension operation ($\hat{u}_{ccw} = 3.2$ V, $\hat{i}_{ccw} = 3.2$ A) and different modulation degrees: a – $\hat{u}_{cw} = 40$ V ($m_a = 0.5$, $n \approx 40\,000$ min^{-1}); b – $\hat{u}_{cw} = 80$ V ($m_a = 0.96$, $n \approx 80\,000$ min^{-1})

A step-like zero-sequence current requirement occurs at 0.5 ms requiring the maximum zero-sequence voltage (positive). Therefore, $d_{7,A}$ and $d_{0,B}$ (all high-side switches of system A on and all low-side switches of system B on) are as big as possible whereas $d_{0,A}$ and $d_{7,B}$ are kept zero. This clearly shows that the remaining zero-voltage time span declines from approximately $T_{sw}/2$ to $T_{sw}/8$. Reciprocally to that, these time spans are kept constantly at their maximum level four times longer at $n/n_N = 4/3$ than at $n/n_N = 2/3$. Consequently, the current rise time is longer for higher modulation degrees. It can be shown approximately that twice the modulation degree leads to a four times longer rise time.

Inherent zero-sequence current with and without control

At high modulation degrees another problem occurs: The zero-sequence current exhibits a 3rd harmonic with regards to the synchronous frequency

disturbing the bearing operation which cannot be counteracted by the current controller since the DC link voltage is too small to realize fast current changes within the short passive voltage instant (compare Fig. 9). Therefore, a third harmonic occurs for modulation degrees $m_a > \sqrt{3}/2$ which is equal to a voltage space vector of length $U_{DC}/2$. For comparison the zero-sequence current $i_{0,non\text{-}control}$ for the case of a symmetrical SVM without zero-sequence current control is given. In order to explain the existence of the third harmonic, Fig. 8 can be consulted. It shows the electric potential of the two star points Z_A, i.e. $u_{\gamma,A}$ and Z_B, i.e. $u_{\gamma,B}$, for the discrete switching states. For the case of block commutation, i.e. $t_{active} = T_{sw}$ and $t_{passive} = 0$, the potential of one star point pulsates between $U_{DC}/6$ and $-U_{DC}/6$ three times per electrical period. The magnitude of the u_0 between the two star points depends on both electric potentials $u_{\gamma,A}$ and $u_{\gamma,B}$. This means, if the two voltage systems are fed in common-mode, no voltage is active between Z_A and Z_B. Therefore, the lateral force generating common-mode voltage system does not lead to a ripple in u_0.
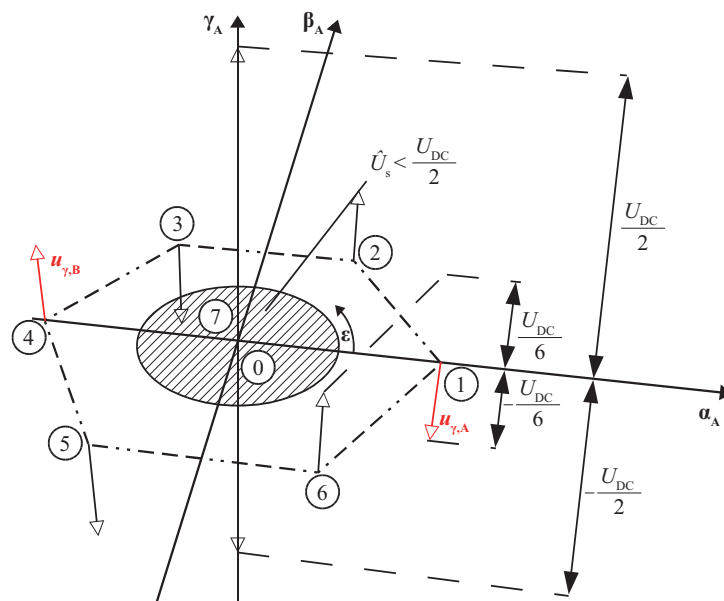
Fig. 8. Switching instants 0, 1, , …, 7 and related electric potentials at the star points Z_A ($u_{\gamma,A}$) and Z_B ($u_{\gamma,B}$) in a 3D (α-β-γ) diagram; red: electric potential $u_{\gamma,A}$ and $u_{\gamma,B}$ at $\varepsilon = 0°$ for differential-mode feeding

However, the differential-mode feeding of u_{cw} leads to a difference in potential, since the two clockwise systems $u_{cw,A}$ and $u_{cw,B}$ are geometrically opposed in the α-β-plane. That is, while system A is e.g. in state 1 ($u_{\gamma,A} = U_{DC}/6$), system B is in instant 4 ($u_{\gamma,B} = -U_{DC}/6$), leading to an amplitude of $u_0 = U_{DC}/3$. A sixth of an electric period later system A is in instant 2 ($u_{\gamma,A} = -U_{DC}/6$), system B is in instant 5 ($u_{\gamma,B} = U_{DC}/6$), leading to an amplitude of $u_0 = -U_{DC}/3$. This pattern continues, so

that for block commutation the voltage drop of the AMB can be given by (14), neglecting the common-mode feeding. Hence, the zero-crossings of this function are at the switching states when the voltage space vector is between two discrete switching states at odd multiples of $\varepsilon = \pi/6$. The maxima of (14) are located at even multiples of $\varepsilon = \pi/6$ (Fig. 8). In order to explain, from which modulation degree this third harmonic occurs, a condition must be found, so that the amplitude of (14) is zero. As explained, only the instants, when the active voltage vector is composed of only one active switching state, must be considered, e.g. $t_{active,A} = t_{1,A}$ and $t_{active,B} = t_{4,B}$. Since $t_{active,A} = t_{active,B}$ due to symmetrical differential-mode feeding, it is obvious that the condition for $u_0 = 0$ must be fulfilled over one switching period by $\overline{u}_{\gamma,A}\big|_{T_{sw}} = 0$ and $\overline{u}_{\gamma,B}\big|_{T_{sw}} = 0$ yielding (15).

$$u_0(t) = \frac{4}{\pi} \cdot \frac{U_{DC}}{3} \cdot \cos(3 \cdot (\omega_s \cdot t - \varepsilon)) \tag{14}$$

By applying (3) and (15), it can be shown that the maximum space vector amplitude is $\hat{U}_s = U_{DC}/2$, i.e. $m_a = \sqrt{3}/2$, which is in accordance with (15). Consequently, it can be said that the system is applicable for $n < 1.25\, n_N$ which is related to a maximum axial force frequency $f_{ax,max}$. This gives an accurate estimation of the maximum applicable modulation degree regardless the exact system parameters. Moreover, the given system meets the shown behavior despite its slightly elliptical voltage space vector orbit, since $\hat{u}_{ccw} \approx 0.05 \cdot \hat{u}_{cw}$.

$$\overline{u}_{\gamma}\big|_{T_{sw}} = \pm \frac{U_{DC}}{6} \cdot t_{active} \mp \frac{U_{DC}}{2} \cdot t_{passive} = 0$$

$$\Rightarrow \quad t_{active} \leq \frac{3}{4} \cdot T_{sw} \wedge t_{passive} > \frac{1}{4} \cdot T_{sw} \quad \Rightarrow \quad \hat{U}_s \leq \frac{U_{DC}}{2} \;;\; m_a \leq \frac{\sqrt{3}}{2} \tag{15}$$

Operating area for variable sinusoidal bearing current

In order to describe the operating area of the axial AMB system it is necessary to point out which requirements the position controller sets for the current controller. The controller design of the thrust magnetic bearing is not in the focus here. However, from the system it is known that an average current of $i_0 = 0.9$ A is needed in order to levitate the rotor if it is operated vertically so that the thrust bearing carries the rotor. From that it is estimated that the maximum zero-sequence current of $i_0 = 3$ A is sufficient even for vertical operation.

In the previous section, it was shown that the slew rate of the current is limited by the inverter voltage rating. This results in a limited operating frequency range for the system: At low frequency, e.g. $i_0 = $ const., the tolerance of the zero-

sequence current in the bearingless motor limits the operation in terms of maximum axial force generation (solid lines in Fig. 9). At high frequency, however, the inverter voltage rating (together with the given time constant of the plant) limits the operation (dashed line in Fig. 9). That is, the current cannot follow the reference signal anymore. If the voltage drop over the plant resistance R_{plant} is neglected the relation between bearing current and required voltage is given by (16) according to [1]. Here, f_{ax} is the bearing current frequency and L_{plant} is the bearing and motor inductance of the circuit.

$$\hat{u}_0 = 2\pi \cdot f_{ax} \cdot L_{plant} \cdot \hat{i}_0 \quad \Rightarrow \quad \hat{i}_0\big|_{\hat{u}_0 = U_{inv,max} = \text{const.}} \sim \frac{1}{f_{ax}} \qquad (16)$$

This shows that the maximum possible bearing current amplitude is inversely proportional to its applied frequency, since the inverter voltage is limited. Usually it is limited by the inverter voltage rating. In this case additionally the modulation degree m_a for the required voltage space vectors of the torque and force generating voltage systems in the bearingless motor has to be considered. Taking into account that the fundamental amplitude of the applied voltage of a square-wave form is $4/\pi \cdot U_{DC}$ the envelope of the peak current $\hat{i}_{0,max}$ can be estimated according to (17) (see Fig. 9).

$$\hat{i}_{0,max} = (1 - m_a) \cdot \frac{2}{\pi^2} \cdot \frac{U_{DC}}{L_{plant}} \cdot \frac{1}{f_{ax}}; \quad \text{where } m_a = \sqrt{3} \cdot \frac{\hat{U}_{cw} + \hat{U}_{ccw}}{U_{DC}} \qquad (17)$$

The black line in Fig. 9 shows the envelope of the operating area at the given conditions (U_{DC} = 150 V, L_{plant} = 15 mH, m_a = 0.73). $i_{0,N}$ = 0,9 A and refers to the current necessary for rotor levitation at vertical operation. $f_{s,N}$ refers to the rated speed of 60 000 min^{-1}. It can be seen that for vertical as well as for horizontal operation the system can be operated without any problems as long as any imbalance force
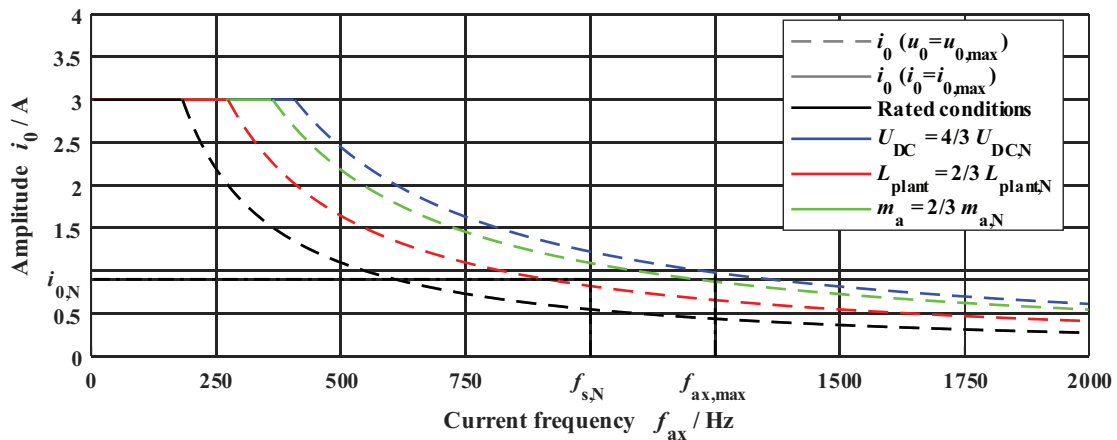
Fig. 9. Simulated operating area of the axial magnetic bearing system

excitation requires less than half the rated bearing current. However, this is not to expect since imbalance forces mainly act radially. Apart from that, there are several options to enlarge the operating area by adapting the system boundary conditions. The most effective is to increase the DC link voltage to increase the current slope and to decrease the modulation degree (blue line in Fig. 9). Another is to operate the drive at lower speeds which requires less modulation degree (green line in Fig. 9) Moreover a decrease in plant inductance yields higher current slopes. However, since $L \sim N^2$ but $F \sim N \cdot I$ a reduction in inductance by means of coil turn reduction is on the costs of moderately higher currents in order to achieve the same bearing force.

CONCLUSIONS

A new method of operating the axial AMB for a cylindrical bearingless machine was introduced which relies on the feeding by the zero-sequence current between the two star points of the machine. Exemplary a 1 kW / 60 000 min^{-1} PM synchronous machine is considered. It was shown that it is possible to manipulate artificially the electric potential of the star point of a three phase winding system by the adaption of the time spans for the passive voltage instants in a SVPWM. However, the voltage drop between the two star points depends on both potentials of the star points, leading to a coupling between the two current systems. It is explained, how this problem of five unknown phase currents can be separated into smaller problems of two and three dimensions. The operation of the system is dependent on the constraints, given by the BM as well as by the inverter capacity.

Firstly, it is shown that a zero-sequence current leads to torque and force ripple and to an increase in eddy current losses in the PM of the rotor. However, all these fields of interest are not crucial for currents $i_0 < 3$ A. For the given AMB the rated current to compensate for the rotor weight is $i_{0,N} = 0.9$ A. So it can be concluded that the constraints by the motor do not determine significantly the applicability of the method. Finally, it is demonstrated that the more crucial constraints are given by the inverter. For pure DC current requirements at steady state and in transient conditions it is shown that the motor currents are not influenced by the zero-sequence current, since the active time spans are calculated independently. For modulation degrees $m_a > 0.866$ a third harmonic occurs in the zero-sequence current, prohibiting operations at speeds $n > 1.25 \cdot n_N$ which is caused by the influence of the active voltage time spans on the star point potential. Finally, the step response and the sinusoidal current requirements yield suitable results for currents $i_0 < 1$ A. Certainly the operating area can be enlarged by a higher DC link voltage, a smaller AMB inductance or if the modulation degree at rated operation is reduced.

Altogether it can be stated that the presented technique is applicable for active magnetic suspensions of high-speed drives, taking into account the mainly non-critical constraints by the bearingless machine and the inverter. It is topic of future investigations to realize the presented technique by a prototype.

References

1. Chiba A, Fukao T, Ichikawa O, Oshima M, Takemoto M, Dorrell DG. *Magnetic Bearings and Bearingless Drives*. 1st ed. Oxford: Elsevier; 2005.

2. Bleuler H, Cole M, Keogh P, Larsonneur R, Maslen E, Nordmann R, Okada Y, Schweitzer G, Traxler A. *Magnetic Bearings – Theory, Design and Application to Rotating Machinery*. Schweitzer G, Maslen EH., editors. Dordrecht Heidelberg London New York: Springer; 2009.

3. Stölting HD, Kallenbach E, Amrhein W, editors. *Handbook of Fractional-Horsepower Drives*. Berlin Heidelberg New York: Springer; 2006.

4. Messager G, Binder A. Evaluation of a Dual Half-Pitched Three-Phase Bearingless High-Speed Permanent Magnet Synchronous Motor Prototype. Proceedings of the 10th ETG/GMM-Symposium Innovative small Drives and Micro-Motor Systems (IKMT); 2015 Sep 14–15; p. 1–6. Cologne, Germany. Berlin Offenbach: VDE Verlag GmbH; 2015.

5. Schneider T, Binder A. Design and Evaluation of a 60 000 rpm Permanent Magnet Bearingless High Speed Motor. Proceedings of the 7th International Conference on Power Electronics and Drive Systems (PEDS); 2007 Nov 27–30; Bangkok, Thailand. IEEE; 2007. doi: 10.1109/peds.2007.4487669

6. Jastrzebski RP, Jaatinen P, Pyrhönen O, Chiba A. Design of 6-slot inset PM bearingless motor for high-speed and higher than 100 kW applications. Proceedings of the 2017 IEEE International Electric Machines and Drives Conference (IEMDC); 2017 May 21–24; p. 1–6. Miami (FL), USA. IEEE; 2017. doi: 10.1109/iemdc.2017.8002143

7. Wang T, Du G, Yu Z, Zhang F, Bai Z. Design and develop of a MW direct drive high-speed permanent-magnet machine for compression. Proceedings of the International Conference on Electrical Machines and Systems (ICEMS); 2013 Oct 26–29; p. 892–895. Busan, South Korea. IEEE; 2013. doi: 10.1109/icems.2013.6713160

8. Mitterhofer H, Amrhein W. Motion control strategy and operational behaviour of a high speed bearingless disc drive. Proceedings of the 6th IET International Conference on Power Electronics, Machines and Drives (PEMD); 2012 Mar 27–29; p. 1–6. Bristol, UK. IET; 2012. doi: 10.1049/cp.2012.0297

9. Bösch PN. *Lagerlose Scheibenläufermotoren höherer Leistung* (*Bearingless disk-like Motors of higher Power Classes*) [dissertation]. Zurich: Swiss Federal Institute of Technology (ETH); 2004.

10. Asama J, Oi T, Oiwa T, Chiba A. Investigation of integrated winding configuration for a two-DOF controlled bearingless PM motor using one three-phase inverter. Proceedings of the 2017 IEEE International Electric Machines and Drives Conference (IEMDC); 2017 May 21–24; p. 1–6. Miami (FL), USA. IEEE; 2017. doi: 10.1109/iemdc.2017.8002219

11. Grabner H, Silber S, Amrhein W. Feedback control of a novel bearingless torque motor using an extended FOC method for PMSMs. Proceedings of the IEEE International Conference on Industrial Technology (ICIT); 2013 Feb 25–28; p. 325–330. Cape Town, South Africa. IEEE; 2013. doi: 10.1109/icit.2013.6505693

12. Steinert D, Nussbaumer T, Kolar JW. Slotless Bearingless Disk Drive for High-Speed and High-Purity Applications. *IEEE Transactions on Industrial Electronics*. 2014; 61(11):5974-5986. doi: 10.1109/TIE.2014.2311379

13. Munteanu G, Binder A, Dewenter S. Five-axis magnetic suspension with two conical air gap bearingless PM synchronous half-motors. Proceedings of the International Symposium on Power Electronics Power Electronics, Electrical Drives, Automation and Motion (SPEEDAM); 2012 Jun 20–22, p. 1246–1251. Sorrento, Italy. IEEE; 2012. doi: 10.1109/speedam.2012.6264414

14. Kascak P, Jansen R, Dever T, Nagorny A, Loparo K. Levitation performance of two opposed permanent magnet pole-pair separated conical bearingless motors. Proceedings of the IEEE Energy Conversion Congress and Exposition; 2011 Sep 17–22; p. 1649–1656. Phoenix (AZ), USA. IEEE; 2011. doi: 10.1109/ecce.2011.6063980

15. Schleicher A, Werner R. Theoretical and experimental analysis of controllability of a novel bearingless rotary-linear reluctance motor with optimal chessboard toothing. Proceedings of the IEEE International Conference on Industrial Technology (ICIT); 2018 Feb 20–22; p. 540–545. Lyon, France. IEEE; 2018. doi: 10.1109/icit.2018.8352234

16. Sugimoto H, Srichiangsa T, Chiba A. Design of a high-speed single-drive bearingless motor. Proceedings of the IEEE International Electric Machines and Drives Conference (IEMDC); 2017 May 21–24; p. 1–6. Miami (FL), USA. IEEE; 2017. doi: 10.1109/iemdc.2017.8002300

17. Gasch R, Nordmann R, Pfützner H. *Rotordynamik* (*Rotor Dynamics*). 2nd ed. Berlin, Heidelberg, New York: Springer; 2006.

18. Munteanu G, Binder A, Schneider T. Development and test of high-speed bearingless PM synchronous machines. *e & i Elektrotechnik und Informationstechnik*. 2011;128(3):75-80. doi: 10.1007/s00502-011-0810-1

19. Messager G, Binder A. Six-axis Rotor Magnetic Suspension Principle for Permanent Magnet Synchronous Motor with Control of the Positive, Negative and Zero-Sequence Current Components. *Applied Computational Electromagnetics Society (ACES) Journal*. 2017;32(8):657-662.

20. Messager G, Binder A. Analytical comparison of conventional and modified winding for high speed bearingless permanent magnet synchronous motor applications. Proceedings of the International Conference on Optimization of Electrical and Electronic Equipment (OPTIM); 2014 May 22–24; p. 330–337. Bran, Romania. IEEE; 2014. doi: 10.1109/optim.2014.6850951

21. Dietz D, Messager G, Binder A. 1 kW / 60 000 min⁻¹ bearingless PM motor with combined winding for torque and rotor suspension. *IET Electric Power Applications*. Forthcoming 2018. doi: 10.1049/iet-epa.2018.0013

22. Schröder D. *Elektrische Antriebe – Regelung von Antriebssystemen*. 4th ed. Berlin Heidelberg: Springer Vieweg; 2015. doi: 10.1007/978-3-642-30096-7_7

23. Binder A. *Elektrische Maschinen und Antriebe – Grundlagen, Betriebsverhalten*. 2nd ed. Heidelberg Dordrecht London New York: Springer; 2018.

24. Sequenz H. *Die Wicklungen elektrischer Maschinen*. 1st ed. Vienna: Springer; 1950.

25. Bergmann G. *Five-Axis Rotor Magnetic Suspension with Bearingless PM Motor Levitation Systems* [dissertation]. Darmstadt: Technical University; 2013.

26. Binder A. Analytical Calculation of Eddy-Current Losses in Massive Rotor Parts of High-Speed Permanent Magnet Machines. Proceedings of the International Symposium on Power Electronics Power Electronics, Electrical Drives, Automation and Motion (SPEEDAM); 2000 Jun 13–16, p. C2-1–C2-6. Ischia, Italy; 2000.

27. Stoll RL. The analysis of eddy currents. Oxford: Clarendon Press; 1974.

28. Greig J, Freeman EM. Travelling-wave problem in electrical machines. *Proceedings of the Institution of Electrical Engineers*. 1967;114(11):1681-1683, doi: 10.1049/piee.1967.0324

Information about the authors:
Dietz Daniel, M.Sc., Landgraf-Georg-Str. 4, 64283 Darmstadt, Germany
E-mail: ddietz@ew.tu-darmstadt.de

Binder Andreas, Prof., Dr.-Ing. habil. Dr. h.c.;
E-mail: abinder@ew.tu-darmstadt.de